



MIT Open Access Articles

Synchronized High-Speed Video, Infrared Thermometry, and Particle Image Velocimetry Data for Validation of Interface-Tracking Simulations of Nucleate Boiling Phenomena

The MIT Faculty has made this article openly available. **Please share** how this access benefits you. Your story matters.

Citation	Duan, X., B. Phillips, T. McKrell, and J. Buongiorno. "Synchronized High-Speed Video, Infrared Thermometry, and Particle Image Velocimetry Data for Validation of Interface-Tracking Simulations of Nucleate Boiling Phenomena." <i>Experimental Heat Transfer</i> 26, no. 2 3 (March 2013): 169-197.
As Published	http://dx.doi.org/10.1080/08916152.2012.736837
Publisher	Taylor & Francis
Version	Author's final manuscript
Citable link	http://hdl.handle.net/1721.1/83904
Terms of Use	Creative Commons Attribution-Noncommercial-Share Alike 3.0
Detailed Terms	http://creativecommons.org/licenses/by-nc-sa/3.0/

Synchronized High-Speed Video, Infrared Thermometry and PIV Data for Validation of Interface-Tracking Simulations of Nucleate Boiling Phenomena

Short title: Synchronized IR, PIV, & HSV for Nucleate Boiling

Xili Duan, Bren Phillips, Thomas McKrell, Jacopo Buongiorno *

Department of Nuclear Science and Engineering, Massachusetts Institute of Technology

* jacopo@mit.edu, 617-253-7316

Abstract

Nucleation, growth and detachment of steam bubbles during nucleate boiling of a water pool at atmospheric pressure is experimentally investigated using a combination of synchronized high-speed video (HSV), infrared (IR) thermography and particle image velocimetry (PIV). The heater is a thin ($<1\ \mu\text{m}$), horizontal ($20\times 10\ \text{mm}^2$), resistively-heated, indium-tin-oxide (ITO) film, vacuum-deposited on a sapphire substrate ($250\ \mu\text{m}$ thick), which allows for unobstructed optical access from below the boiling surface. This approach enables detailed measurement of the phase, temperature and velocity distributions on and above the boiling surface. The database reported herein is for isolated bubbles, exhibiting nucleation temperatures $107\text{-}109^\circ\text{C}$, bubble departure diameters $3.0\text{-}3.8\ \text{mm}$, frequencies $4.7\text{-}15.00\ \text{Hz}$, wait and growth times $52\text{-}200\ \text{ms}$ and $15\text{-}16\ \text{ms}$, respectively, at average heat fluxes $29\text{-}36\ \text{kW/m}^2$. The database is most useful for validation of modern simulations of nucleate boiling in which the phase, temperature and velocity distributions within and around bubbles are resolved using interface capturing methods such as Volume Of Fluid (VOF), Level Set (LS) and Front Tracking (FT).

1 Introduction

Liquid-vapor multi-phase flow and heat transfer phenomena (e.g., boiling, condensation, stratification, flashing, critical flow, etc.) are critical to the operation and safety of many engineering systems, e.g.

nuclear reactors, conventional power plants, high-power electronics, just to mention a few. Nucleate boiling in particular is one of the most studied physical processes in science and engineering. At low heat flux, where isolated bubble growth occurs, the ebullition cycle can be qualitatively described as follows [1]. Once the liquid layer above the heater surface reaches the superheat required to activate a given nucleation site, a bubble begins to form and pushes the surrounding liquid outward, except for a thin liquid microlayer that remains in contact with the wall underneath the bubble. Evaporation occurs at the bubble surface and through the microlayer, thus fueling further bubble growth. When the size of the bubble is sufficiently large, buoyancy (and/or drag in flow boiling) causes the bubble to detach from the surface; new fresh liquid floods the surface, and the cycle starts over.

In modeling nucleate boiling heat transfer, researchers have been relying on speculative hypotheses for decades. For example, the widely popular Rohsenow's correlation is based on the assumption that single-phase convection and nucleate boiling are analogous physical processes, and can be both correlated in terms of the Reynolds and Prandtl number of the liquid phase; for nucleate boiling the characteristic velocity and length are assumed to be the downward liquid velocity and the most unstable Taylor wavelength, respectively; then, an empirical constant is determined to fit the experimental data for any fluid/surface combination [2]. In general, the tools used to simulate multiphase flow and heat transfer phenomena are still highly empirical, and make use of over-simplified assumptions; in particular, the geometry of the vapor/liquid interface is always idealized (e.g., smooth or sinusoidal wavy liquid films, spherical or elliptic droplets and bubbles, etc.), and then the ubiquitous two-fluid six-equation approach is used with empirical interfacial exchange terms [3].

Transformational advancements in *multi-phase* Computational Fluid Dynamics (CFD) are available through the use of Interface Tracking Methods (ITMs). ITMs do not assume an idealized vapor-liquid interface topology, but rather calculate it from 'first principles'. A marker function C is introduced, shown in Eq. (1), its value being zero if vapor is present at position \vec{r} at time t , and one if liquid is present.

$$C(\vec{r},t) \equiv \begin{cases} 1 & \text{liquid} \\ 0 & \text{vapor} \end{cases} \quad (1)$$

The marker function, which effectively defines the interface between the two phases, is predicted by a topology equation shown in Eq. (2) [4].

$$\frac{\partial C}{\partial t} + \vec{u} \cdot \nabla C = \frac{\dot{m}}{\rho} \delta_s \quad (2)$$

where \vec{u} is the velocity vector of the interface, \dot{m} is the phase-change rate, ρ is the density and δ_s is the Dirac delta function at the interface. Different ITMs differ in how the topology equation is solved; the state-of-the-art approaches are Volume Of Fluid (VOF) [5-7], Level Set (LS) [8,9] and Front Tracking (FT) [10,11]. ITMs are coupled with an appropriate ‘flow solver’ for the velocity, pressure and temperature fields. In the presence of turbulence, various approaches are possible such as Direct Numerical Simulation (DNS), Large Eddy Simulation (LES), or Unsteady Reynolds Averaged Navier Stokes (URANS). The reader is referred to the enormous amount of information about these methods which can be found in the CFD literature. Since the velocity and temperature gradients near the interface can be resolved, prediction of the exchange of momentum, mass and heat at the interface in principle requires no empirical correlations. Examples of ITM simulations performed with the code TransAT (Ascomp GmbH) are shown in Figure 1. It can be seen that in all cases the interface can be resolved quite sharply.

In the past decade several research groups have conducted ITM-based simulations of nucleate boiling, most notably Son et al. [13], Abarajith and Dhir [14], Dhir [15,16], Son and Dhir [17], Stephan and Kunkelmann [18], Kunkelmann and Stephan [19], Ose and Kunugi [20,21], Mukherjee and Kandlikar [22], Tryggvason et al. [23], Juric et al. [24], Caviezel et al. [25], Narayanan et al. [26]. A few examples from these studies are shown in Fig. 2.

Time-resolved temperature distribution data for the boiling surface and direct visualization of the bubble cycle are needed for validation of these ‘first principle’ simulations of bubble nucleation and growth. However, gathering the detailed data needed for validation of advanced simulation models is not straightforward. The traditional approaches based on thermocouples and high-speed visualization of the boiling process suffer from several shortcomings; for example, the thermocouples can only measure temperature at discrete locations on the boiling surface, thus little information on the temperature *distribution* about a nucleation site can be obtained. Thermocouples have relatively long response time, thus are generally unsuitable for studying the bubble nucleation and growth phenomena, which have time scales of the order of milliseconds. However, **micro-thermocouples with very fast response time [27], and temperature sensors with high spatial resolution [28] have been developed.**

The usefulness of high-speed video is typically limited by poor optical access to the nucleation site and interference from adjacent bubbles. **To obtain unobstructed view of the boiling process from below the boiling surface, Chung and No [29], Nishio and Tanaka [30], and Chu et al. [31] used the total reflection approach, which requires a heater that is completely transparent to visible light and a silicon oil layer underneath.**

Second-generation two-phase flow diagnostics, such as multi-sensor conductivity and optical probes [32,33] and wire-mesh probes [34], can measure bubble diameter and velocity near the boiling surface. However, these approaches are intrusive, and also produce data only at discrete locations within the boiling fluid. It was not until the early 2000s that new possibilities for generating time-resolved multi-dimensional data on the bubble nucleation and growth cycle have opened up with the introduction of infrared-based visualization of thermal patterns on the boiling surface by Theofanous et al. [35]. At MIT we have expanded the infrared (IR) thermography approach by synchronizing it with high-speed video (HSV) from *below* the boiling surface [36]. **IR-based temperature mapping of boiling surfaces has been reported also by Wagner and Stephan [37] and Golobic et al. [38], and very recently by Kim et al. [39], Golobic et al. [40] and Kunkelmann et al. [41]. Kim and Buongiorno [42,43] developed the DETection of**

Phase by Infrared Thermometry (DEPIcT) technique, which uses the differences in emissivity of the liquid and vapor phases to measure the phase distribution (including the shape of the microlayer) on the boiling surface of IR-transparent heaters. Finally, Demiray and Kim [44] developed a powerful approach to resolving the local instantaneous surface heat flux, which is based on arrays of micro-heaters, individually controlled to achieve a constant temperature boundary condition.

In this paper we present a new approach which combines synchronized IR, HSV (from the side of the boiling surface) and particle image velocimetry (PIV). The objective of this study is to present a small but detailed database for validation of the numerical simulations, not necessarily to cast new light on the physical phenomena. The limited range of conditions explored (heat generation rate, materials, wall superheats, fluid pressure and temperature) is consistent with this objective.

2 Experimental Apparatus

Figure 3 shows a schematic of the pool boiling facility used in this study. It includes a boiling cell, a HSV camera, a PIV system, a high-speed IR camera, and other auxiliary equipment. A brief description of each major subsystem follows.

2.1 Boiling cell

The boiling cell features a concentric-double- cylinder structure: boiling of deionized (DI) water takes place in the inner cell, while the outer enclosure functions as an isothermal bath. The temperature (and thus degree of subcooling) of the water in the inner cell is controlled by circulating a temperature-controlled fluid through the isothermal bath. The heater unit sits at the bottom of the cell and accommodates heater samples of a special design described in Section 2.2 below. There are four glass windows spaced equally at 90° along the outer surface of the boiling cell. Two adjacent windows are for

the laser illumination and PIV imaging, respectively. A reflux condenser is installed through a hole in the center of the inner cell cover to maintain pressure and prevent reduction of water inventory in the boiling cell. Thermocouples are inserted into the inner cell and the isothermal bath, to monitor the bulk temperatures of the fluids. All the metal parts are made of stainless steel grade 316, to minimize corrosion.

2.2 ITO heater

Boiling occurs on a specially designed heater installed in the inner boiling cell (Figure 4). The heating element is an ITO layer of 0.7 μm thickness vacuum deposited onto a 250 μm thick sapphire substrate. The sapphire substrate has a size of 50 x 50 mm^2 , while the exposed heating area of ITO is 20 x 10 mm^2 . Silver electrode pads of 20 μm thickness are used for DC power supply to the heater.

The ITO heating element is in contact with the water and is resistively heated. In the experiments, voltage and current across the ITO heater are measured and the heat generation rate per unit area is calculated as $q=V \cdot I/A_{heater}$. The bottom surface of the sapphire substrate is exposed to air. The ITO is transparent in the visible range (380-750 nm), but opaque in the mid-IR (3-5 μm) range, while the sapphire substrate is transparent in both the visible and mid-IR ranges. This combination allows temperature measurement on the bottom of the ITO layer with the high speed IR camera. Because the ITO heater is so thin, the temperature drop across the ITO is negligible, so the IR camera effectively measures the temperature of the boiling surface. The static contact angle of water on ITO is of the order of 80-90° as measured (at room temperature) on the actual heaters in the facility.

2.3 PIV system

In the PIV system, a high repetition Nd:YLF laser (Photonics Industries, Model DM20-527) is used to

illuminate the seed particles in the fluid. A compact adjustable light sheet optics unit on the laser head produces a visible green (527 nm wavelength) laser sheet less than 0.5 mm thick. The laser has pulse energy of 20 mJ at 2000 Hz, with pulse duration of 180 ns. The pulse repetition rate can be up to 10 kHz, although 2000 Hz was used in most of our PIV measurement (with some experiments running at 3000 Hz and 5000 Hz). The fluid in the inner boiling cell is seeded with a type of fluorescent particles- Fluoro-Max, polymer microspheres of 3.2 μm and mass density 1.05 g/cm^3 . A Phantom 12.1 high speed video camera (Vision Research) is used for imaging the boiling process. The camera's CMOS sensor is 25.6 x 16.0 mm^2 with 20 μm pixel size. An AF Micro-Nikkor 200 mm f/4D lens (Nikon) is used for "close-up" imaging of the flow fields around a single bubble. The long working distance of the lens allows for the camera to be placed safely away from the experiment, and when used with extension rings can achieve spatial resolutions of better than 15 μm . The PIV analysis software DaVis 7.2 (LaVision) is used for imaging and velocity analysis. It also enables setup of the high-speed controller to control the timing of the laser and high speed cameras. In the velocity analysis, interrogation area size of 32 x 32 pixels is mainly used in our measurement, with 50% overlap for cross correlation. This gives a spatial resolution of about 0.48 mm for the velocity vectors.

2.4 IR camera and IR thermometry

A SC6000 high-speed infrared camera (FLIR Systems) is used to record the temperature distribution on the heater surface. The sensor of the IR camera captures mid-IR (in the 3-5 μm wavelength range) radiation from the ITO heater surface, which is reflected to the view of IR camera through a gold coated mirror, as shown in Figure 3. The camera sensor detects the infrared radiation intensity and outputs the signal as pixel counts. The calibration leads to a counts-temperature curve to be used for conversion of the intensity image to temperature fields. A 100 mm germanium lens (f/2.3) with a 3/4" extension ring was used to achieve the desired spatial resolution at the optimal camera distance from the reference plane. The IR camera has a maximum resolution of 640 x 512 pixels. In the experiment, only a small window

(e.g. 224 x 116) is needed for imaging the whole ITO heater surface, allowing for a high frame rate of 1000 fps. For measurement of a single bubble, even higher frame rate can be achieved; frame rates up to 3000 fps were used in the experiment.

2.5 *Experimental procedure*

After cleaning the inner cell, a fresh ITO heater is installed. The inner cell is then filled with distilled water or DI water. The circulation heater is set to the desired temperature for the isothermal bath. It usually takes up to 65 minutes to heat up the boiling cell from room temperature to 100°C and degas it. Then the ITO heater is powered to reach the desired heat flux for nucleate boiling. The IR camera is focused to the ITO heater plane and its imaging window is adjusted to include the chosen nucleation site. When the PIV laser is used, the positioning and distance between the laser head and the ITO heater is also adjusted so that (i) the laser sheet is illuminating the plane of the chosen nucleation site, and (ii) the waist of the laser sheet (where it is the thinnest) is just above the nucleation site. This ensures good illumination and imaging of the bubble behavior. PIV and IR image acquisition is started when cyclic conditions are reached in the boiling process - after several ebullition cycles.

The high speed controller produces transistor-transistor logic (TTL) pulses (with desired frequency set in the DaVis software), which trigger both the IR and PIV system to simultaneously record IR and PIV images, allowing the synchronization of both cameras' image sequences. Alternatively, the IR camera can send out a trigger signal to the PIV system for the synchronization.

3 Experimental Database

Two datasets were generated in the pool boiling facility shown in Figure 3. Saturated de-ionized water was used in the experiments. The first dataset contains data from synchronized high-speed video (HSV)

and Infrared (IR) thermometry measurements. The second dataset contains experimental data from synchronized Particle Imaging Velocimetry (PIV) and IR measurements.

3.1 Dataset 1 (HSV-IR)

The dataset is for three consecutive bubbles from the same nucleation site. Basic experimental conditions are as follows:

- (1) Water temperature and pressure: $99.5 \pm 1.1^\circ\text{C}$ (bulk) and 101 kPa.
- (2) Planar heat generation rate of the ITO heater: $q=28.7 \pm 0.6 \text{ kW/m}^2$.
- (3) HSV frame rate: 7204 fps; IR frame rate: 2401.3 fps. Therefore, there is an IR image for every three HSV images. HSV and IR are synchronized within $3 \mu\text{s}$, as determined by calibration with visible and IR LEDs controlled by a function generator.
- (4) The nucleation temperature for all three bubbles, as measured by the IR camera, is $109.0 \pm 2^\circ\text{C}$. This nucleation temperature would correspond to a nucleation site (microcavity) of critical radius $\sim 3 \mu\text{m}$, **as estimated using the Young-Laplace and Clausius-Clapeyron equations [45].**

3.1.1 HSV bubble images

HSV images of the bubbles emerging from the nucleation site (view from a side window of the boiling cell) were taken to reveal bubble diameter, bubble shape and bubble frequency. Table I shows nine representative images, and thus shape, of each of the three consecutive bubbles. Time zero is the instant of bubble nucleation. Note the initial hemispherical shape, typical of the inertia-controlled growth phase, followed by vertical elongation and necking of the bubble base (air balloon shape), typical of the heat-diffusion-controlled growth phase. After the bubble departs from the surface, the shape is wobbling elliptical, which is expected for steam bubbles of this size ($E\ddot{o}=2.2$, $Mo=3 \times 10^{-13}$). Lateral and vertical dimensions of these three bubbles are given as functions of time in Fig. 5. Three basic dimensions of the

bubbles were measured, i.e. base diameter (D_{i_base}), lateral diameter ($D_{i_lateral}$), and height (Height i), $i=1$ to 3 for the bubbles. The height is measured from the heater surface to the top of the bubble. **The equivalent bubble departure diameter, D_e , calculated by integration of the bubble profile along the bubble axis of symmetry, is 3.8 ± 0.07 mm.** The repeatability from bubble to bubble is excellent.

3.1.2 IR measurement of heater surface temperature

The temperature measurements were synchronized with the HSV images to allow for an integrated examination of the bubble dynamics. Table II shows representative examples of the temperature field corresponding to the HSV images of Bubble 1 in Table I. Very similar results were obtained for Bubbles 2 and 3, and are not reported here. Note the development of a ‘cold ring’ corresponding to the microlayer region, and a central ‘hot spot’ corresponding to the dry base of the bubble, followed by the progressive temperature recovery of the surface, a sign of the reconstruction of the thermal boundary layer after bubble departure.

The surface temperature data were also averaged azimuthally about the nucleation site, to get the time-

dependent radial distribution of temperature, $T(r,t) \equiv \frac{1}{2\pi} \int_0^{2\pi} T(r,\varphi,t) d\varphi$, shown in Figure 6 for all three

bubbles. The microlayer cold ring is evident also from these plots. Again note the repeatability of the data. Figure 7 shows the temperature history of the nucleation site, which readily reveals the bubble frequency (~ 4.7 Hz), wait time (~ 200 ms) and growth time (~ 15 ms).

The average heat transfer coefficient for the nucleation site, \bar{h} , was calculated according to Eq. (3).

$$\bar{h} = q / (\bar{T}_{wall} - T_{sat}) \quad (3)$$

where $q=28.7$ kW/m² is the imposed planar heat generation rate, $T_{sat}=99.5^{\circ}\text{C}$ and

$\bar{T}_{wall} \equiv \frac{1}{t_{cycle}} \int_0^{t_{cycle}} dt \frac{1}{A} \int_A T dA$ is the time- and space-averaged temperature of the wall obtained from the IR

data, t_{cycle} is the duration of one ebullition cycle, and A is taken to be a circle of radius R centered at the nucleation site. The results are shown in Figure 8 where the average heat transfer coefficient (calculated over 3 ebullition cycles) is plotted versus R . **We resisted the temptation to calculate the instantaneous distribution of the heat flux to the fluid via solution of the heat equation in the substrate, as is often done in the literature [27-28,36-38], because it introduces additional large uncertainties, especially when conduction in the direction perpendicular to the wall is neglected even in cases when the heater is thermally “thick” or is in contact with an unheated substrate which is thick. A notable exception is the microheater approach [44] in which the local heat flux is directly measured.**

3.2 Dataset 2 (PIV-IR)

The dataset is for three consecutive bubbles from the same nucleation site. Basic experimental conditions are as follows:

- (1) Water temperature and pressure: 99.0 ± 1.1 °C (bulk) and 101 kPa.
- (2) Planar heat generation rate of the ITO heater: $q=36.0 \pm 0.7$ kW/m²
- (3) PIV imaging frame rate: 2000 fps; IR imaging frame rate: 1000 fps. Therefore, there is an IR image for every two HSV images. PIV and IR are synchronized within 350 μs . Time zero is the instant of bubble nucleation.
- (4) The nucleation temperature for all three bubbles, as measured by the IR camera, is $107.4 \pm 2^{\circ}\text{C}$. This nucleation temperature would correspond to a nucleation site (microcavity) of radius ~ 4 μm .

3.2.1 PIV measurement of fluid velocity around bubbles

In the PIV system, the HSV camera takes images of the fluid from a side window of the test cell, in the same way as previously discussed for Dataset 1. **The equivalent bubble departure diameter for Dataset 2 is 3.0 ± 0.05 mm, smaller than in Dataset 1.**

The PIV measurement results are presented in two formats. First, each frame of raw PIV image was saved as a *.jpg picture, which reveals the bubble shape as well as the 2D fluid velocity distribution, shown as velocity vectors. The velocity scale is established by a color bar scale superimposed on the images. Second, the measured velocity data was saved as *.dat files, with each frame of velocity field as one *.dat file. Each file is then a 2D map of the velocity components (V_x , V_y) at different locations in the flow field, noted as (x/position1, y/position 2).

Table III shows representative PIV-measured velocity vectors at different times for all three bubbles in Dataset 2. Note the expected radially-symmetric velocity field during the bubble growth period, followed by the typical vortices in the bubble wake upon bubble departure from the heater. In these results, the accuracy of the velocity measurement is ± 3 mm/s, as stated by the PIV vendor. A benchmark flow test is underway to further refine the estimate of our PIV system accuracy.

Quantitative information about the velocity vectors along the interface of the growing/rising bubbles can also be extracted from the PIV data. Figure 9 shows the distribution of the fluid velocity magnitude and angle along the bubble interface (Bubble 1 is used in this example). The velocity magnitude is calculated

as $V = \sqrt{V_x^2 + V_y^2}$, while the angle is $\beta = \tan^{-1}(V_y/V_x)$. **The velocity magnitude is generally higher at**

the front (top) portion of the bubble and lower at both sides in the lateral direction where two wakes are generated. During its initial growth period, the hemispherical bubble pushes all the liquid around it and therefore creates higher fluid velocity (e.g. at 5 ms). This bubble expansion effect decreases at the end of bubble growth so the liquid velocity actually shows a decrease trend towards bubble departure. At the later period of bubble rising, the liquid velocity increases at both the front (top) and rear (bottom) portion

due to the bubble's rapid rise. The velocity direction is almost perpendicular to the bubble profile, except in the wake regions.

3.2.2 IR measurement of heater temperature

IR data presentation follows the same format as for Dataset 1 (Section 3.1.2 above). Table VI shows examples of temperature distributions synchronized to their corresponding PIV images for Bubble 1 in Table III.

Figure 10 shows representative temporal and spatial variations of the temperatures beneath each of the three consecutive bubbles. Figure 11 shows the time history of the nucleation site, from which the bubble frequency (~15 Hz), wait time (~52 ms) and growth time (~16 ms) can readily be evaluated.

Figure 12 shows the average heat transfer coefficient for the nucleation site as a function of the domain size over which the average is performed. Here it is $q=36.0 \text{ kW/m}^2$, $T_{sat}=99.0^\circ\text{C}$ and again \bar{T}_{wall} is from the IR data averaged over 3 ebullition cycles.

4 Discussion

A comparison of the data presented above with previous studies suggests that our bubbles are fairly prototypical. For example, they exhibit the expected initial hemispherical growth, typical of the inertia-controlled phase, followed by elongation in the vertical direction during the heat-diffusion controlled phase [45]. The bubbles in Dataset 1 have a higher departure diameter than those in Dataset 2, i.e. 3.8 mm and 3.0 mm respectively. This is no surprise as the Dataset 1 bubbles have a higher nucleation temperature (109 vs 107°C), thus thicker and hotter thermal boundary layer. The experimental values of

the bubble departure diameters are bracketed by the traditional correlations of Fritz [46] ($D_e \sim 4.2-4.7$ mm), Ruckenstein [47] ($D_e \sim 2.8-3.6$ mm) and Jensen and Memmel [48] ($D_e \sim 0.8-1.0$ mm) for the conditions of interest.

The wait time for the bubbles in Dataset 2 is also much shorter than for Dataset 1, which is due to the differences in heat generation rate (driving the reconstruction of the thermal boundary layer) and nucleation temperature (setting the end point of the wait period). Traditional wait time models cannot be used in our case because they assume either a constant wall temperature [49] or a uniform volumetric heat generation rate within the substrate [50], whereas in our experimental apparatus heat generation takes place only in the thin (submicronic) ITO layer at the wall/fluid interface. If we assume that reconstruction of the thermal boundary layer following bubble departure is a transient conduction problem, and approximate the fluid and the solid substrate as semi-infinite walls with a constant heat generation rate per unit area, q , localized at their interface, it can be easily shown that the wall temperature $T_w(t)$ is proportional to q and to the square root of time, shown in Eq. (4), where the constant of proportionality depends only on the thermophysical properties of the fluid and solid substrate, which do not change in our experiments.

$$T_w(t) - T_i \propto q\sqrt{t} \quad (4)$$

Here T_i is the wall temperature at the beginning of the wait period, which can be found directly from Figures 7 and 11, $T_i \sim 104.4^\circ\text{C}$ for Dataset 1 and $\sim 103.5^\circ\text{C}$ for Dataset 2. The wait time ends when T_w equals the temperature of nucleation, $T_n \sim 109^\circ\text{C}$ for Dataset 1 and $\sim 107.4^\circ\text{C}$ for Dataset 2. Therefore we can find the wait time by solving for t in Eq. (4) and is shown in Eq. (5).

$$t_{wait} \propto \left[\frac{T_n - T_i}{q} \right]^2 \quad (5)$$

Using the experimental values of T_n , T_i and q , Eq. 5 predicts a reduction of the wait time of 55% from Dataset 1 to Dataset 2, in reasonable agreement with the actual measured reduction $(200-52)/200 \approx 74\%$.

Interestingly, the growth time is about the same for both datasets, i.e. 15 and 16 ms for Dataset 1 and Dataset 2 respectively. We speculate it is due to the conflicting effects of nucleation temperature (the higher the nucleation temperature, the faster the growth) and departure diameter (the higher the departure diameter, the longer the growth time). Therefore, the Dataset 1 bubbles with their high nucleation temperature and bubble departure diameter have about the same growth time as the smaller Dataset 2 bubbles. The measured values of the growth time are bracketed by the predictions of the growth time models of Hatton and Hall [50] (7-8 ms) and Zuber [51] (38-88 ms).

The cooling effect of the microlayer underneath the bubbles in Dataset 1 is clearly visible in the IR images in Tables II and IV and then quantitatively in the temperature plots in Figures 6 and 10. The radial displacement of the temperature minimum is ~ 0.1 m/s, which compares well with the 0.05-0.20 m/s range measured by direct observation of the radial displacement of the microlayer edge for nucleate boiling of water at atmospheric pressure by Koffman and Plesset [52], Voutsinos and Judd [53], and Kim and Buongiorno [42].

The velocity profiles in Tables III through V confirm the initial, nearly isotropic radial expansion of the bubble captured by the HSV. Then a strong fluid recirculation occurs in the wake of the bubble after departure. This recirculation is usually referred to as micro-convection or bubble agitation and has been attributed a significant amount of heat transfer from the heating surface [49,54]. However, a plot of the fluid vorticity (Figure 13) suggests that agitation near the wall decays off very rapidly after bubble departure: the fluid comes to rest within ~ 10 ms after bubble departure vs. a total wait period of about ~ 52 ms. Therefore, the main effect of bubble departure on heat transfer is likely not micro-convection, but rather the local displacement of the thermal boundary layer with subsequent transient conduction during the wait period. This latter phenomenon has long been thought to be a very significant heat transfer mechanism in nucleate boiling [55-57].

The time-averaged heat transfer coefficient plots in Figures 8 and 12 are also interesting, as they give an indication of the so-called area of influence of an isolated bubble over the whole ebullition cycle. If we take the inflection point in the heat transfer coefficient plots as a measure of the area of influence, then it can be seen that for Datasets 1 and 2 the area of influence has a radial extension (measured from the nucleation site location) of about 1.3 and 0.8 mm, respectively, thus somewhat smaller than the bubble radius at departure in each dataset, in agreement with the findings of Moghaddam and Kiger [28] and Kunkelmann et al. [41]. In the past some researchers had recommended areas of influence as extensive as two radii of departure [56].

Finally, the rising velocity of the bubbles after departure, which can be estimated from the HSV images of Tables I and III, ranges from 0.17 m/s (Dataset 2) to 0.19 m/s (Dataset 1). The observed shape of these bubbles is wobbling elliptical. This compares well with the expected shape and velocity (0.14 - 0.15 m/s) for bubbles of $E\ddot{o} = 1.4-2.3$ and $Mo = 3 \times 10^{-13}$, as estimated from the $E\ddot{o}$ - Mo - Re chart [58].

5 Conclusions

Synchronized high-speed video, infrared thermography and particle image velocimetry were used to study nucleation, growth and detachment of isolated bubbles in nucleate pool boiling of water at atmospheric pressure and moderate heat flux. Data included measurements of bubble size and shape vs. time, bubble departure frequency, wait and growth times, as well as 2D temperature history of the heater surface and velocity distribution within the liquid surrounding the bubbles. All the expected features of the ebullition cycles could be confirmed, i.e. initial hemispherical growth, followed by vertical elongation, a dependence of the wait time on nucleation temperature and heat generation rate, a strong cooling effect

underneath the growing bubbles due to the presence of an evaporating microlayer, a rapidly decaying fluid recirculation near the wall following bubble departure, an area of influence which extends to approximately one bubble radius around the nucleation site, etc. In summary, the bubbles analyzed here seem to be a good representative sample of the isolated-bubble regime of nucleate boiling. Comparison of some measured quantities with the respective predictions of traditional models and correlations have confirmed this conclusion quantitatively.

The data can be used to validate mechanistic simulations of nucleate boiling in which the 3D vapor/liquid interface is captured and the flow field is resolved. However, the usefulness of this database is not limited to such approaches. Data for nucleation site density, bubble departure diameter, frequency, wait and growth times are a necessary input also for the source terms in interfacial area transport models [3], CFD ‘multi-fluid’ models [59-62], and semi-empirical models of boiling heat transfer, such as the heat flux partitioning model [63], Kolev’s bubble interaction model [64] or the more recent hybrid numerical-empirical model presented in [65].

6 Acknowledgements

This work was supported by the U.S. Department of Energy under the Consortium for Advanced Simulation of LWRs (CASL) program. The U.S. National Science Foundation and the Natural Science and Engineering Research Council of Canada are also gratefully acknowledged for Mr. Phillips’ graduate fellowship and Dr. Duan’s postdoctoral fellowship, respectively.

7 Nomenclature

Variable	Definition	Units
A	Wall domain for temperature average	m^2
A_{heater}	Heater surface	m^2
C	Marker function	/
D_d	Bubble departure diameter	m
$Eö$	Eotvos number	/
\bar{h}	Average heat transfer coefficient	$\text{kW}/\text{m}^2\text{K}$
I	Current	A
M	Morton number	/
\dot{m}	Phase change rate	$\text{kg}/\text{m}^2\text{s}$
q''	Planar heat generation rate	kW/m^2
r	Radial coordinate from center of bubble base	m
\vec{r}	Position vector	m
R	Radial size of domain for temperature average	m
t	Time	s
t_{cycle}	Ebullition cycle	s
T_i	Wall temperature at the start of the wait period	$^{\circ}\text{C}$
T_n	Nucleation temperature	$^{\circ}\text{C}$
T_{sat}	Saturation temperature	$^{\circ}\text{C}$
\bar{T}_{wall}	Average wall temperature	$^{\circ}\text{C}$
\vec{u}	Velocity vector	m/s
V	Voltage	V

V_x, V_y	Components of velocity vector	m/s
α	Angular position at interface	Degrees
β	Direction of velocity vector	Degrees
δ_s	Dirac-delta function at interface	1/m
φ	Azimuthal coordinate on wall surface	Degrees
ρ	Density	kg/m ³

8 References

- [1] Y.Y. Hsu, R.W. Graham, Transport Processes in Boiling and Two-Phase Systems, American Nuc. Soc., Inc., Illinois, USA, 1986.
- [2] W.M. Rohsenow, A method of correlating heat transfer data for surface boiling of liquids, Trans. ASME, 74, 969, 1952.
- [3] M. Ishii and T. Hibiki, Thermo-fluid dynamics of two-phase flow, Springer, 2006.
- [4] D. Lakehal, M. Meier and M. Fulgosi, Interface tracking towards the direct simulation of heat and mass transfer in multiphase flows, Int. J. Heat and Fluid Flow, vol. 23, pp. 242-257, 2002.
- [5] W. J. Rider and D. B. Kothe, Reconstructing volume tracking, J. Comp. Phys., vol. 141, pp. 112-152, 1998.
- [6] M. Rudman, A volume-tracking method for incompressible multifluid flows with large density variations, Int. J. Numer. Meth. Fluids vol. 28, pp. 357–378, 1998.
- [7] R. Scardovelli and S. Zaleski, Direct numerical simulation of free-surface and interfacial flow, Ann. Rev. Fluid Mech., vol. 31, pp. 567-603, 1999.
- [8] S. J. Osher and R. P. Fedkiw, Level set methods: An overview and some recent results, J. Comp. Phys., Vol. 169, pp. 463-502, 2001.
- [9] J. A. Sethian, Evolution, implementation and application of level set and fast marching methods for advancing fronts, J. Comp. Phys., vol. 169, pp. 503-555, 2001.
- [10] G. Tryggvason, B. Bunner, A. Esmaeeli, D. Juric, N. Al-Rawahi, W. Tauber, J. Han, S. Nas and Y.-J. Jan, A front tracking method for the computations of multiphase flow, J. Comp. Phys., vol. 169, pp. 708-759, 2001.
- [11] J. Du, B. Fix, J. Glimm, X. Jia, X. Li, Y. Li and L. Wu, A simple package for front tracking, J. Comp. Phys., vol. 213, pp. 613-628, 2006.
- [12] P. Liovic and D. Lakehal, Interface-turbulence interactions in large-scale bubbling processes, Int. J. Heat and Fluid Flow, vol. 28, pp. 127-144, 2007.

- [13] G. Son, N. Ramanujapu, V. K. Dhir, Numerical simulation of bubble merger process on a single nucleation site during pool nucleate boiling, *Journal of Heat Transfer*, vol. 124, no.1, pp. 51-62, 2002.
- [14] H. S. Abarajith and V. K. Dhir, A numerical study of the effect of contact angle on the dynamics of a single bubble during pool boiling, IMECE2002-33876, Proceedings of IMECE-2002, ASME International Mechanical Engineering Congress & Exposition, November 17-22, 2002, New Orleans, Louisiana.
- [15] V. K. Dhir, Mechanistic prediction of nucleate boiling heat transfer - Achievable or a hopeless task?, *J. Heat Transfer*, vol. 128, no. 1, 1-12, 2006.
- [16] G. Son, V. K. Dhir, Numerical Simulation of Nucleate Boiling on a Horizontal Surface at High Heat Fluxes, *Int. J. Heat Mass Transfer*, vol. 51, no. 9-10, pp. 2566-2582, 2007.
- [17] V. K. Dhir, Simulation of boiling – how far we have come!, ECI International Conference on Boiling Heat Transfer, Florianópolis-SC-Brazil, 3-7 May 2009.
- [18] P. Stephan and C. Kunkelmann, CFD Simulation of Boiling Flows Using the Volume-Of-Fluid Method within OpenFoam, ECI International Conference on Boiling Heat Transfer, Florianópolis, Brazil, 3-7 May 2009.
- [19] C. Kunkelmann and P. Stephan, Numerical simulation of the transient heat transfer during nucleate boiling of refrigerant HFE-7100, *International Journal of Refrigeration*, vol. 33, no. 7, pp. 1221-1228, November 2010.
- [20] Y. Ose and T. Kunugi, Numerical Simulation on Subcooled Pool Boiling, , Paper No. MN-10, 6th International Symposium on Multiphase Flow, Heat Mass Transfer and Energy Conversion, Xi'an, China, 11-15 July 2009.
- [21] Y. Ose and T. Kunugi Numerical Prediction on Subcooled Boiling Bubble Behavior, Paper 530, 14th Int. Topical Meeting on Nuclear Reactor Thermalhydraulics, NURETH-14, Toronto, Ontario, Canada, September 25-30, 2011.
- [22] Mukherjee, A. and Kandlikar, S. G., Numerical Study of Single Bubbles with Dynamic Contact Angle During Nucleate Pool Boiling, *Int. J. Heat Mass Transfer*, vol. 50, no. 1-2, pp. 127-138, 2007.
- [23] G. Tryggvason, S. Thomas, and J. Lu, Direct Numerical Simulations of Nucleate Boiling, IMECE2008-67444, Proceedings of IMECE-2008, 2008 ASME International Mechanical Engineering Congress and Exposition Boston, Massachusetts, USA, October 31-November 6, 2008.
- [24] D. Juric, S. Shin and G. Tryggvason, Direct Numerical Simulations of Nucleate Boiling, 6th International Conference on Multiphase Flow, ICMF 2007, Leipzig, Germany, July 9-13, 2007.
- [25] D. Caviezel, C. Narayanan, D. Lakehal, T-N. Dinh, Coarse-Grained Micro-Hydrodynamics Simulation of High Heat-Flux Boiling Using the CMFD Code TransAT, Paper CHT-08-402,

- Proceedings of CHT-08, ICHMT International Symposium on Advances in Computational Heat Transfer, Marrakech, Morocco, May 11-16, 2008.
- [26] C. Narayanan, S. Thomas, D. Lakehal, Statistical Modeling of Bubble Nucleation and Heat Transfer Using Interface Tracking in Transat CMFD Code, Proceedings of the 3rd Joint US-European Fluids Engineering Summer Meeting & 8th International Conference on Nanochannels, Microchannels and Minichannels FEDSM2010-ICNMM2010, Montreal, Quebec, Canada, August 1-4, 2010, FEDSM2010-ICNMM2010-30139.
- [27] Y. Heng, A. Mhamdi, S. Gross, A. Reusken, M. Buchholz, H. Auracher, W. Marquardt, Reconstruction of local heat fluxes in pool boiling experiments along the entire boiling curve from high resolution transient temperature measurements, *Int. J. Heat Mass Transfer*, vol. 51, pp. 5072-5087, 2008.
- [28] S. Moghaddam and K. Kiger, Physical mechanisms of heat transfer during single bubble nucleate boiling of FC-72 under saturation conditions-I. Experimental investigation, *Int. J. Heat Mass Transfer*, vol. 52, 1284-1294, 2009.
- [29] H. J. Chung, H. C. No, Simultaneous visualization of dry spots and bubbles for pool boiling of R-113 on a horizontal heater, *International Journal of Heat and Mass Transfer* 46 2239–2251, 2003.
- [30] S. Nishio and H. Tanaka, Visualization of Boiling Structures in High Heat-Flux Pool- Boiling, *Int. J. Heat Mass Transfer*, vol. 47, pp. 4559-4568, 2004.
- [31] I.-C. Chu, H. C. NO, C.-H. Song, Observation of High Heat Flux Boiling Structures in a Horizontal Pool by a Total Reflection Technique, Paper 401, 14th International Topical Meeting on Nuclear Reactor Thermal Hydraulics (NURETH-14), Toronto, Ontario, Canada, September 25-29, 2011.
- [32] E. Barrau, N. Rivière, Ch. Poupot and A. Cartellier, Single and double optical probes in air-water two-phase flows: real time signal processing and sensor performance, *Int. J. Multiphase Flow*, vol. 25, no.2, pp. 229-256, 1999.
- [33] S. Kim, X. Y. Fu, X. Wang and M. Ishii, Development of the miniaturized four-sensor conductivity probe and the signal processing scheme, *Int. J. Heat Mass Transfer*, vol. 43, no. 22, 4101-4118, 2000.
- [34] H. M. Prasser, A. Bottger, J. Zschau, A new electrode-mesh tomography for gas–liquid flows, *Flow Measurement and Instrumentation*, vol. 9, pp. 111-119, 1998.
- [35] T. G. Theofanous, J. P. Tu, A. T. Dinh and T. N. Dinh, The Boiling Crisis Phenomenon, *J. Experimental Thermal Fluid Science*, P.I: pp. 775-792, P.II: pp. 793-810, vol. 26, no. 6-7, 2002.

- [36] C. Gerardi, J. Buongiorno, L. W. Hu, T. McKrell, Study of Bubble Growth in Water Pool Boiling through Synchronized, Infrared Thermometry and High-Speed Video, *International Journal of Heat and Mass Transfer*, vol. 53, 19-20 4185-4192, 2010.
- [37] E. Wagner and P. Stephan, High-resolution measurements at nucleate boiling of pure FC-84 and FC-3284 and its binary mixtures, *Journal of Heat Transfer*, vol. 131, no. 12, p. 121008, 2009.
- [38] Golobic, J. Petkovsek, M. Baselj, A. Papez, D.B.R. Kenning, Experimental determination of transient wall temperature distributions close to growing vapour bubbles, *Heat Mass Transfer*, vol. 45, 857–866, 2009.
- [39] T. H. Kim, E. Kommer, S. Dessiatoun, J. Kim, Measurement of two-phase flow and heat transfer parameters using infrared thermometry, *Int. J. Multiphase Flow*, vol. 40, 56–67, 2012.
- [40] Golobic, J. Petkovsek, D.B.R. Kenning, Bubble growth and horizontal coalescence in saturated pool boiling on a titanium foil, investigated by high-speed IR thermography, *Int. J. Heat Mass Transfer*, vol. 55, 1385–1402, 2012.
- [41] C. Kunkelmann, K. Ibrahim, N. Schweizer, S. Herbert, P. Stephan, T. Gambaryan-Roisman, The effect of three-phase contact line speed on local evaporative heat transfer: Experimental and numerical investigations, *Int. J. Heat Mass Transfer*, vol. 55, 1896–1904, 2012.
- [42] H. Kim, J. Buongiorno, Detection of Liquid-Vapor-Solid Triple Contact Line in Two-Phase Heat Transfer Phenomena Using High-Speed Infra-Red Thermometry, *Int. J. Multiphase Flow*, vol. 37, 166-172, 2011.
- [43] H. Kim, J. Buongiorno, An Infrared-Based Experimental Technique to Detect Phase Dynamics on Boiling Surfaces, *Nuc. Eng. Design*, under review, 2012.
- [44] F. Demiray, J. Kim, Microscale heat transfer measurements during pool boiling of FC-72: effect of subcooling, *Int. J. Heat Mass Transfer*, vol. 47, pp. 3257-3268, 2004.
- [45] V. P. Carey, *Liquid-Vapor Phase-Change Phenomena*, Taylor and Francis, 2nd Ed., 2008.
- [46] W. Fritz, Berechnung des Maximalvolumen von Dampfblasen, *Phys. Z.*, vol. 36, pp 379-388, 1935.
- [47] E. Ruckenstein, Physical model for nucleate boiling heat transfer from a horizontal surface, *Bul. Institutului Politeh. Bucuresti*, vol. 33, no 3, pp 79-88; *Appl. Mech. Rev.* 16, Rev. 6055, 1963.
- [48] M.K. Jensen, G.J. Memmel, Evaluation of bubble departure diameter correlations, *Proc Eighth Int. Heat Transf. Conf.*, 4, pp. 1907-1912, 1986.
- [49] Y. Y. Hsu and R. W. Graham, An Analytical and Experimental Study of the Thermal Boundary Layer and Ebullition Cycle in Nucleate Boiling, *NASA TND-594*, 1961.
- [50] A. P. Hatton and I. S. Hall, Photographic Study of Boiling on prepared Surfaces, *Proc. 3rd Int. Heat Transfer Conference*, Chicago, IV, 24-37, 1966.

- [51] N. Zuber, The Dynamics of Vapor Bubbles in Non-uniform Temperature Fields, *Int. J. Heat Mass Transfer*, vol. 2, pp. 83-98, 1961.
- [52] L. D. Koffman and M. S. Plesset, Experimental observations of the microlayer in vapor bubble growth on a heated solid, *Journal of Heat Transfer*, vol. 105, p.625, 1983.
- [53] C. M. Voutsinos and R. L. Judd, Laser interferometric investigation of the microlayer evaporation phenomenon, *Journal of Heat Transfer*, vol. 97, p. 88, 1975.
- [54] Y. Y. Hsu and R. W. Graham, *Transport Processes in Boiling and Two-phase Systems*, Chps. 5 and 6, Hemisphere, New York, 1976.
- [55] H. K. Forster and R. Greif, Heat transfer to boiling liquid, mechanism and correlations, *Trans AMS J Heat Transfer*, vol. 81, pp. 43-53, 1959.
- [56] C. Y. Han and P. Griffith, The mechanism of heat transfer in nucleate pool boiling, Part I, Bubble initiation, growth and departure, *Int. J. Heat Mass Transfer*, vol. 8, no. 6, 887-904, 1965.
- [57] B. B. Mikic and W. M. Rohsenow, A new correlation of pool boiling data including the effect of heating surface characteristics, *Trans. ASME J. Heat Transfer*, vol. 91 p. 245, 1969.
- [58] Clift, R., Grace, J. R., and Weber, M. E., *Bubbles, Drops and Particles*, Academic Press, New York, 1978.
- [59] D. Bestion et al., Some lessons learned from the use of Two-Phase CFD for Nuclear Reactor Thermalhydraulics, N13-P1139, *Proc. of NURETH-13*, Kanazawa, Japan, September 27-October 2, 2009.
- [60] W. K. In and T.-H. Chun, CFD Analysis of a Nuclear Fuel Bundle Test for Void Distribution Benchmark, N13-P1259, *Proc. of NURETH-13*, Kanazawa, Japan, September 27-October 2, 2009.
- [61] S. Lo, A. Splawski and B. J. Yun, The Importance of Correct Modeling of Bubble Size and Condensation in Prediction of Sub-Cooled Boiling Flows, Paper # 75, *NURETH-14*, Toronto, Ontario, Canada, September 25-30, 2011.
- [62] E. Michta, K. Fu, H. Anglart and K. Angele, Numerical Predictions of Bubbly Two-Phase Flows with Openfoam, Paper # 617, *NURETH-14*, Toronto, Ontario, Canada, September 25-30, 2011.
- [63] N. Kurul, M.Z. Podowski, Multidimensional effects in forced convection subcooled boiling, *Proc. 9th International Heat Transfer Conference*, Jerusalem, Israel. pp. 21-25, 1990.
- [64] N. Kolev, How accurately can we predict nucleate boiling?, in *Multiphase Flow Dynamics 2*, Springer, 2002.

- [65] Sanna, C. Hutter, D.B.R. Kenning, T.G. Karayiannis, K. Sefiane, R.A. Nelson, Nucleate Pool Boiling Investigation on a Silicon Test Section with Micro-Fabricated Cavities, ECI International Conference on Boiling Heat Transfer, Florianópolis, Brazil, 3-7 May, 2009.

TABLES

Table I - Representative HSV images of growing and departing bubbles in Dataset 1.

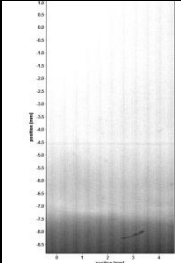
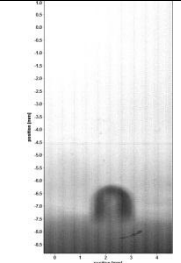
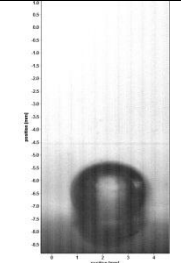
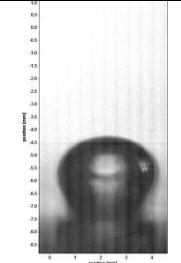
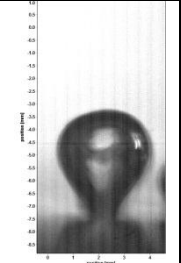
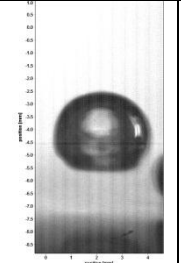
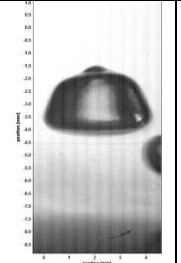
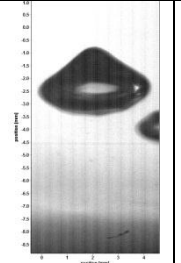
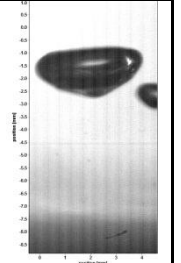
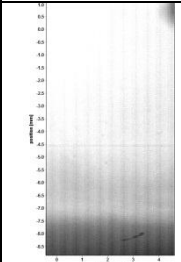
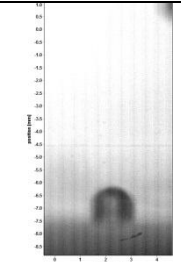
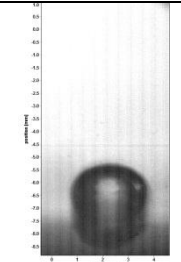
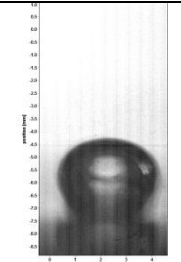
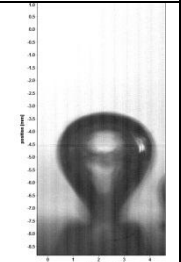
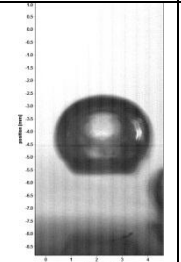
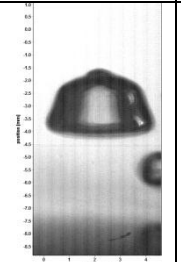
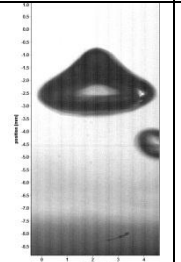
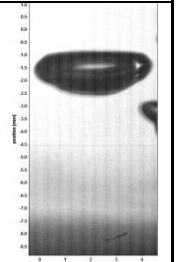
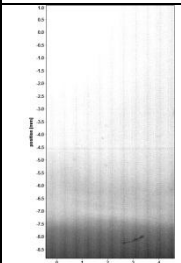
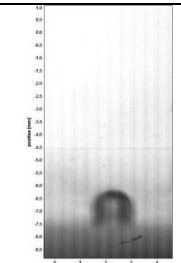
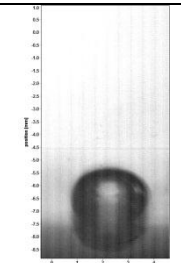
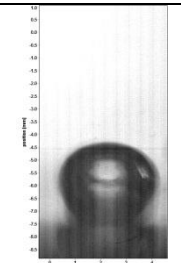
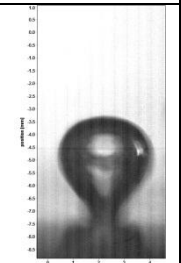
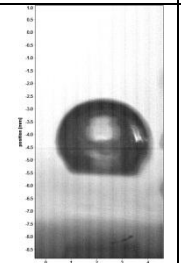
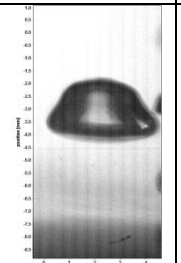
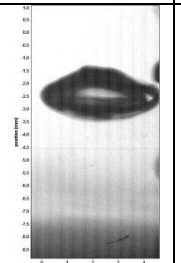
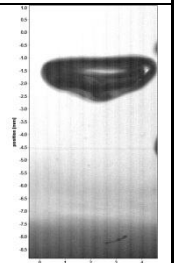
Time (ms)	0 (bubble nucleation)	0.7	2.8	6.9	13.2	17.3	22.9	27.1	31.2
Bubble 1									
Bubble 2									
Bubble 3									

Table II - Synchronized HSV and IR results for Bubble 1 in Dataset 1. The temperature scale is in °C.

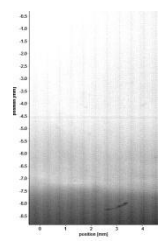
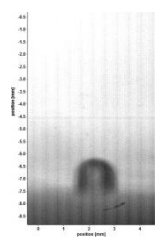
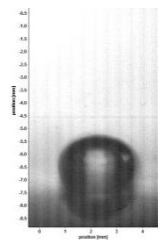
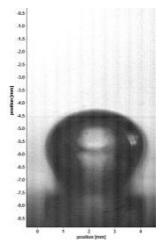
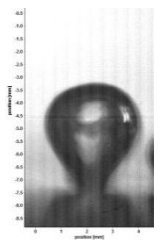
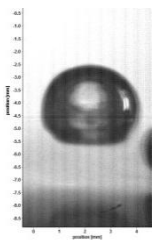
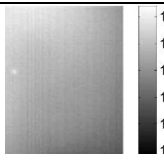
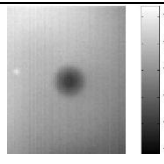
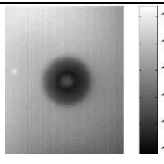
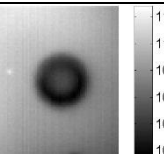
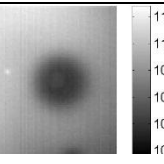
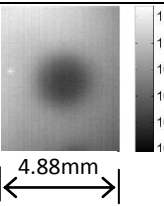
Time (ms)	0 (bubble nucleation)	0.7	2.8	6.9	13.2	17.3
HSV images						
IR images						

Table III - Representative PIV images of the growing and departing Bubble 1 in Dataset 2

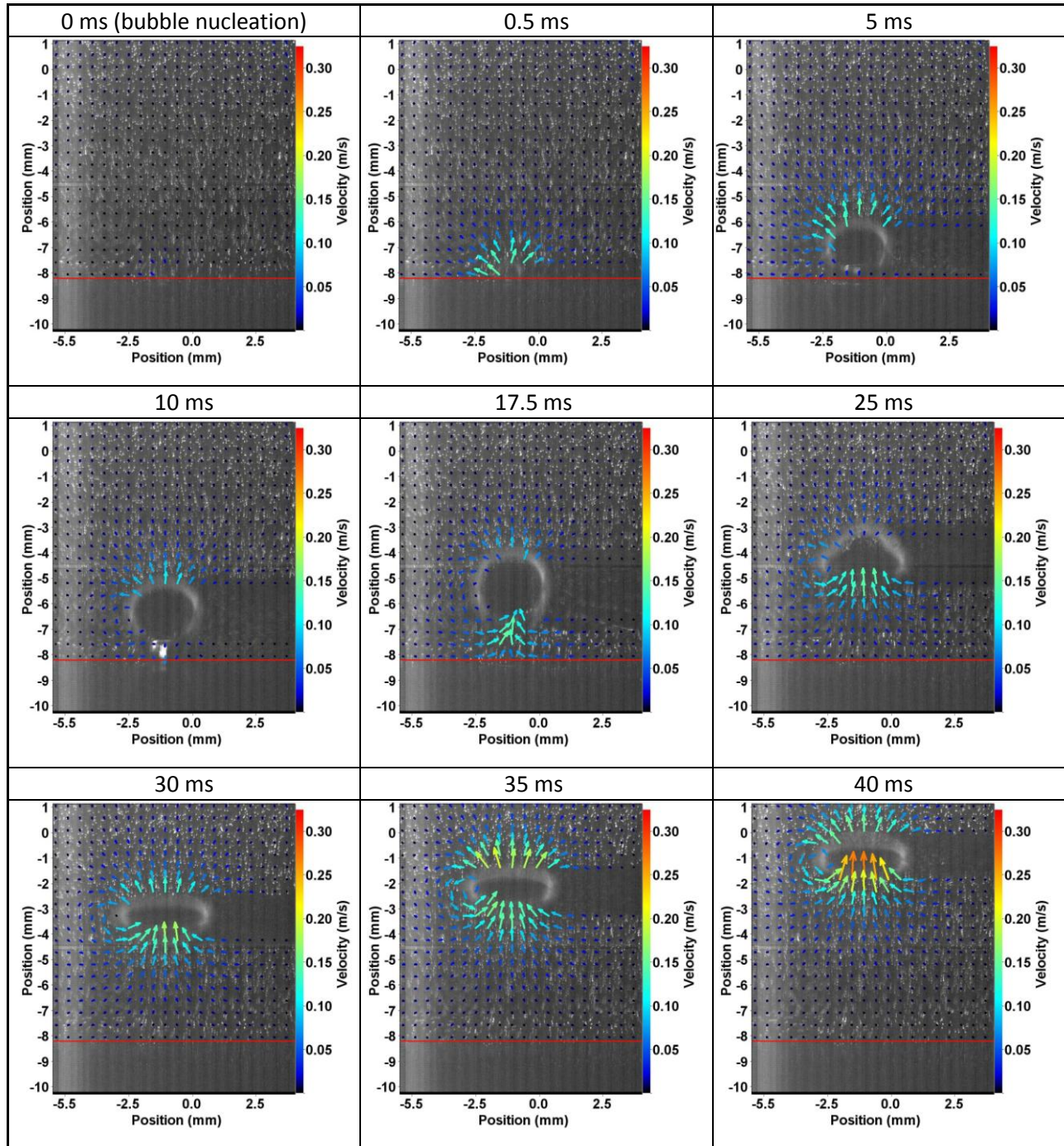


Table IV - Representative PIV images of the growing and departing Bubble 2 in Dataset 2

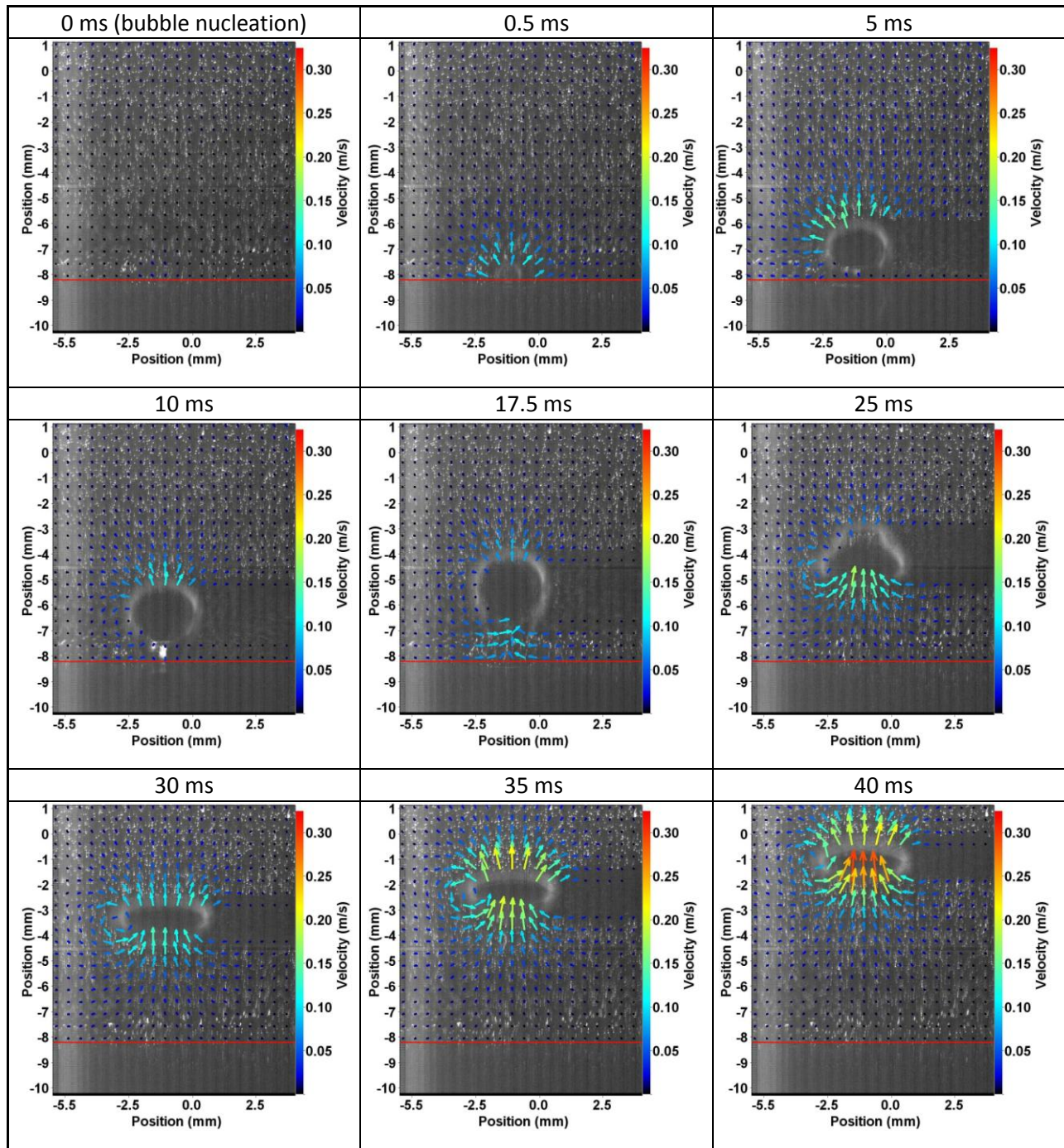


Table V - Representative PIV images of the growing and departing Bubble 3 in Dataset 2

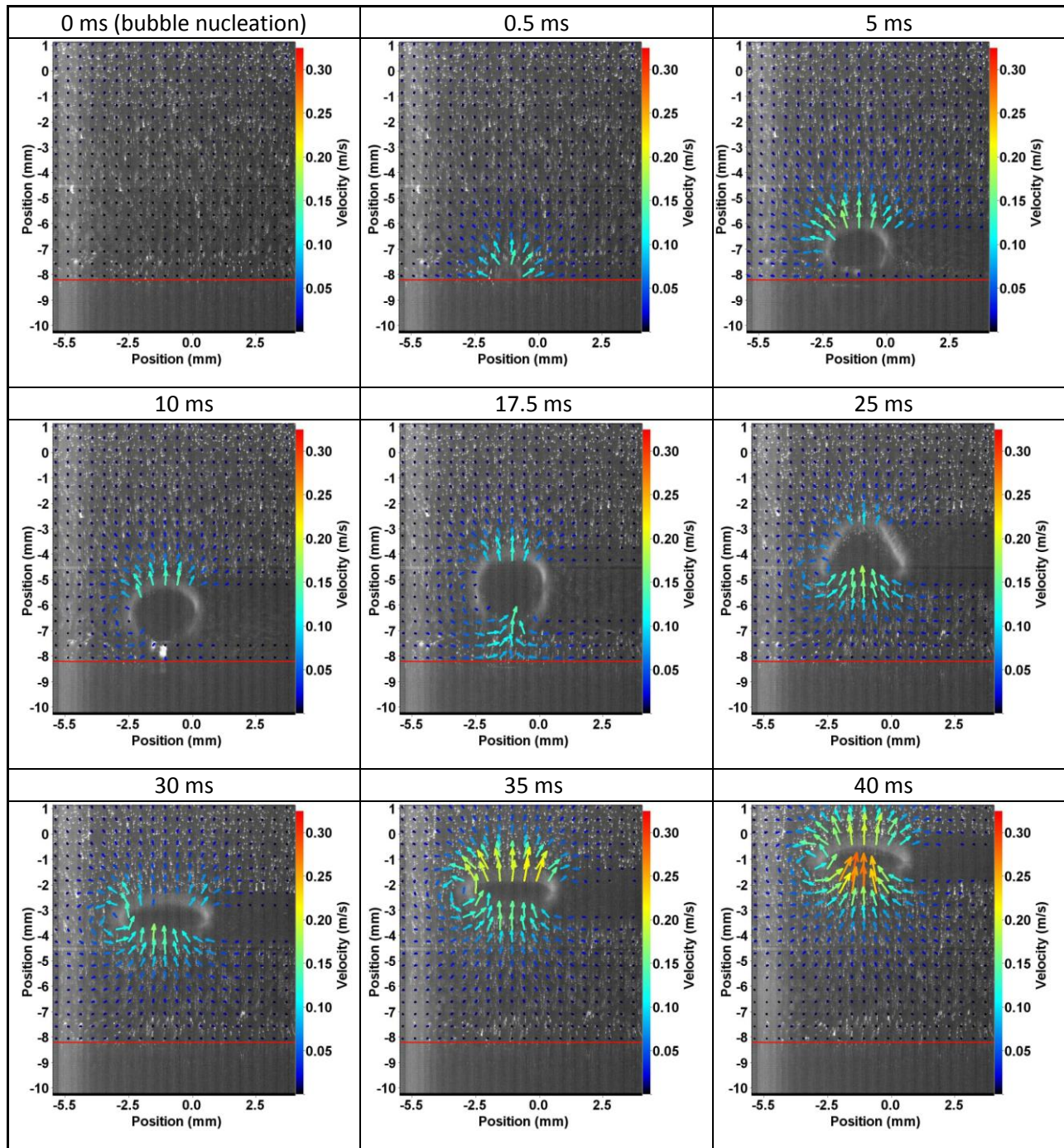
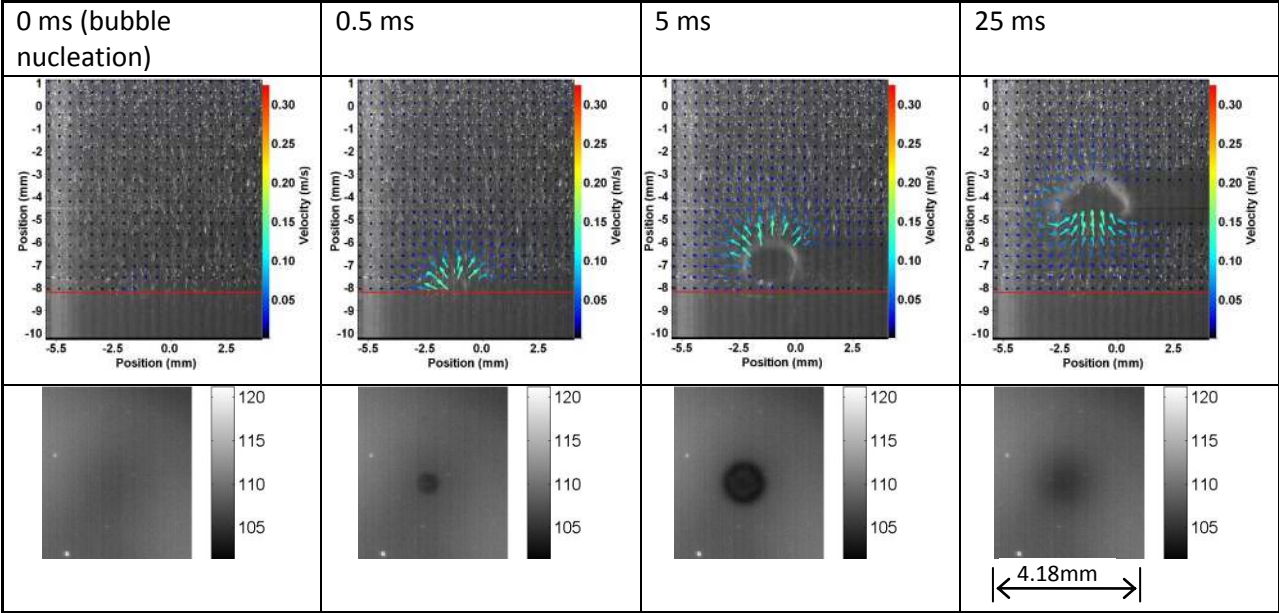


Table VI - Synchronized PIV and IR measurements for Bubble 1, Dataset 2. The temperature scale is in °C.



FIGURES

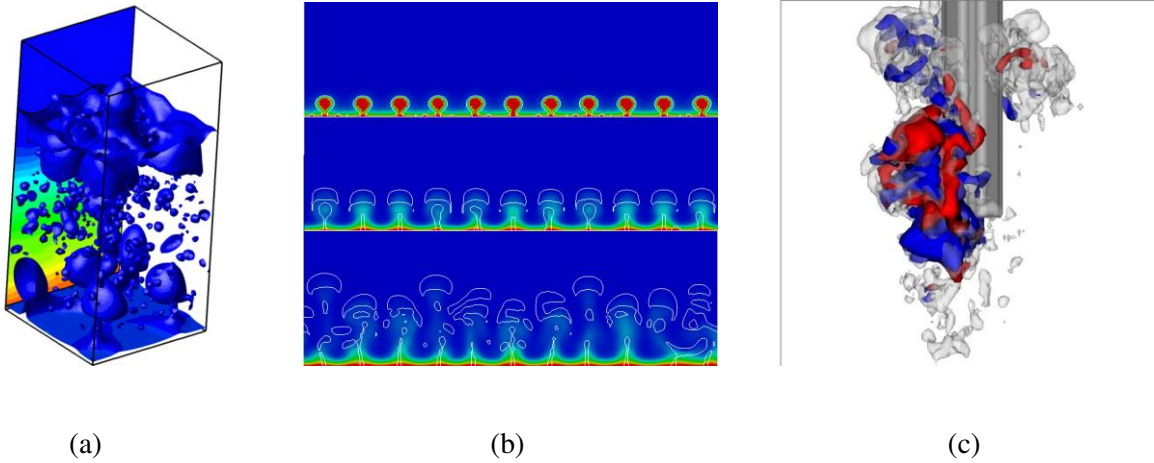
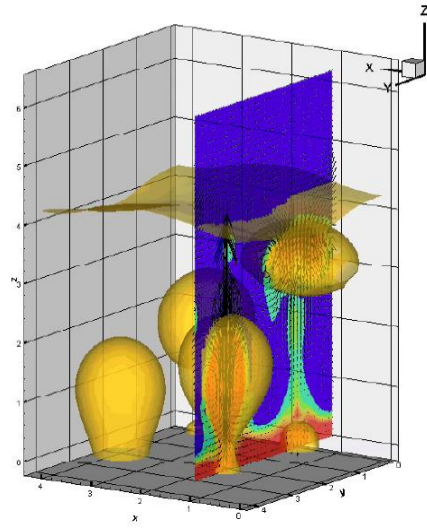
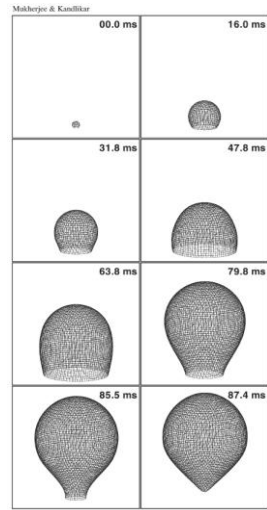


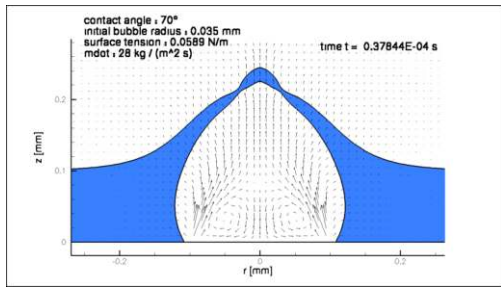
Figure 1. (a) LS simulation of film boiling from a flat surface in a reduced domain (courtesy of Ascomp GmbH), (b) LS simulation of film boiling from a flat surface in a wider domain, showing more heterogeneous topology modes at various instants (courtesy of Ascomp GmbH), and (c) LES-VOF simulation of gas injection in a BWR suppression pool of water [12].



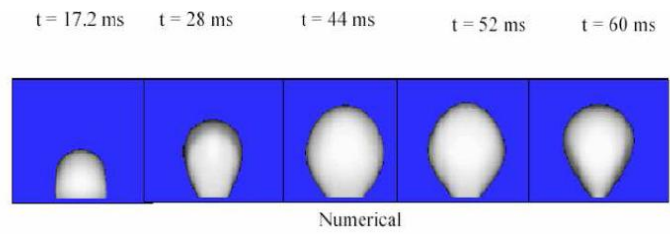
(a)



(b)



(c)



(d)

Figure 2. Numerical simulations of nucleate boiling using (a) FT [24], (b) LS [22], (c) LS [25], and (d) LS [17].

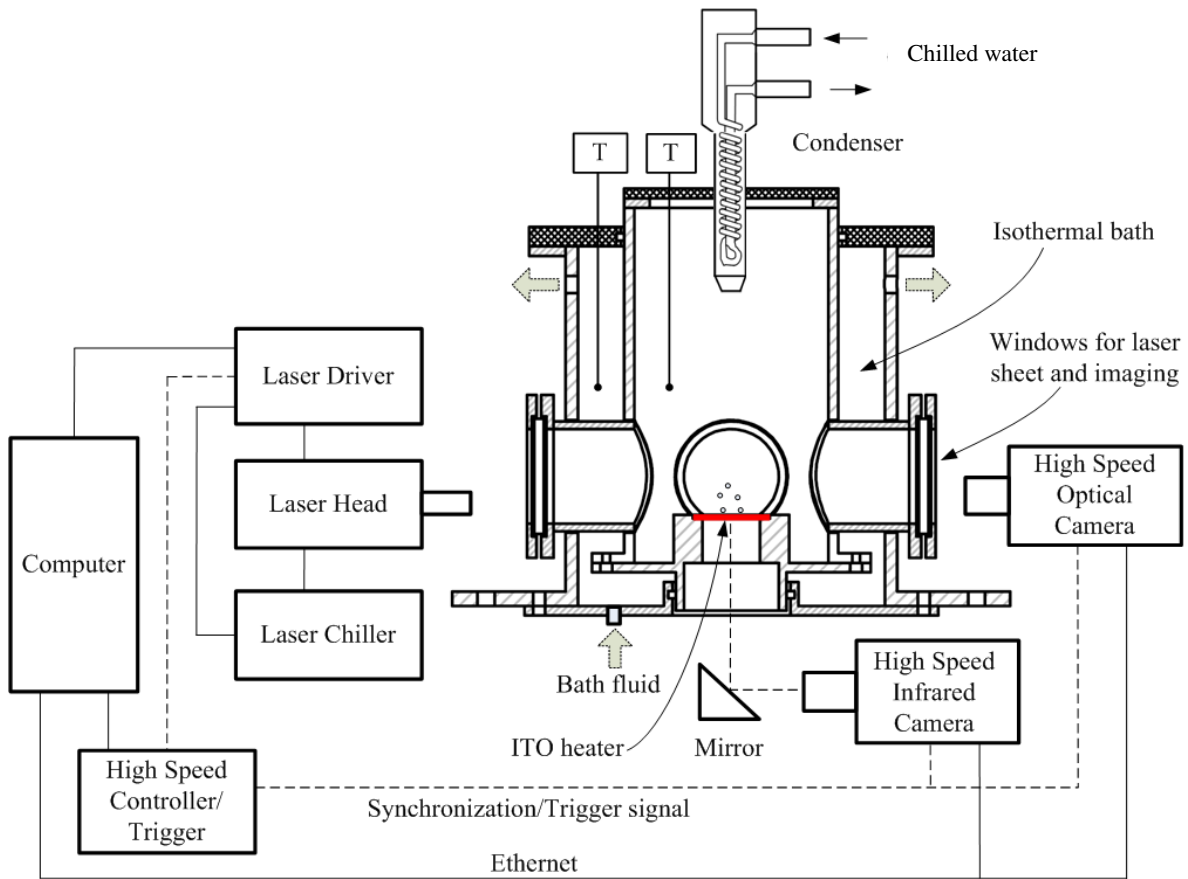


Figure 3. Schematic of the boiling facility with PIV and infrared thermometry systems.

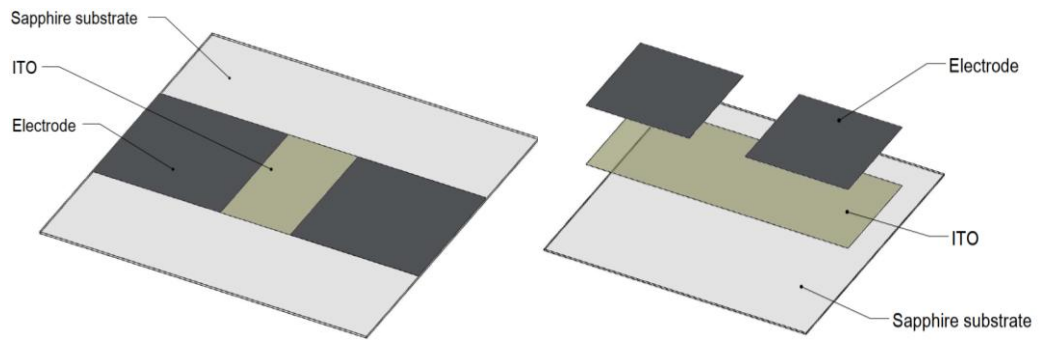


Figure 4. Schematic of the ITO heater.

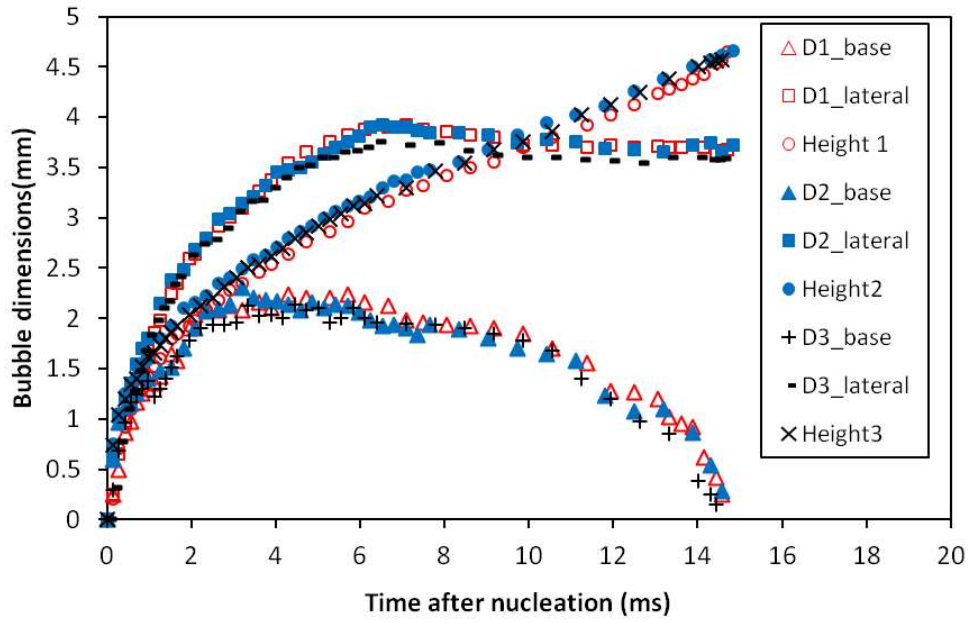
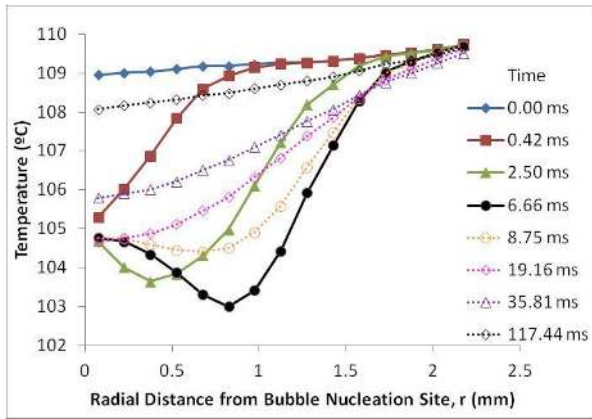
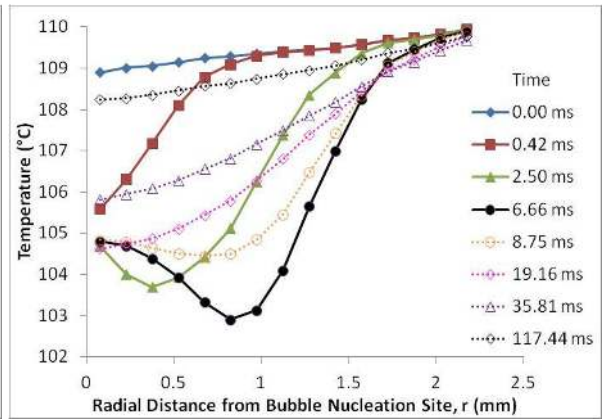


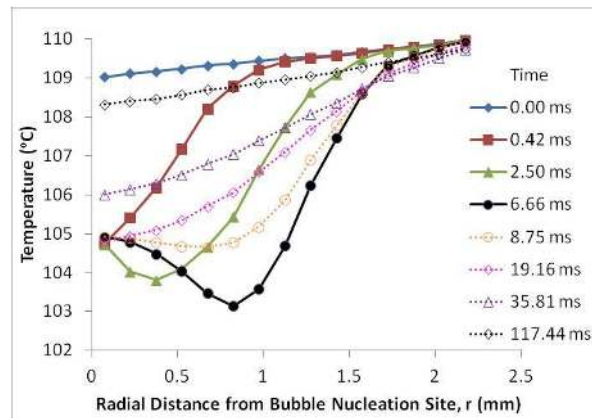
Figure 5 – Dimensions of three consecutive bubbles in Dataset 1. The measurement of the bubble dimensions has an accuracy of ± 0.04 mm (error bars not shown).



(a) Bubble 1



(b) Bubble 2



(c) Bubble 3

Figure 6 – Temperature distribution on the heater surface about the nucleation site of interest for the three consecutive bubbles in Dataset 1. Time is in milliseconds. The accuracy of measured temperature is

$\pm 2^\circ\text{C}$; the precision is $< 0.5^\circ\text{C}$. (error bars not shown)

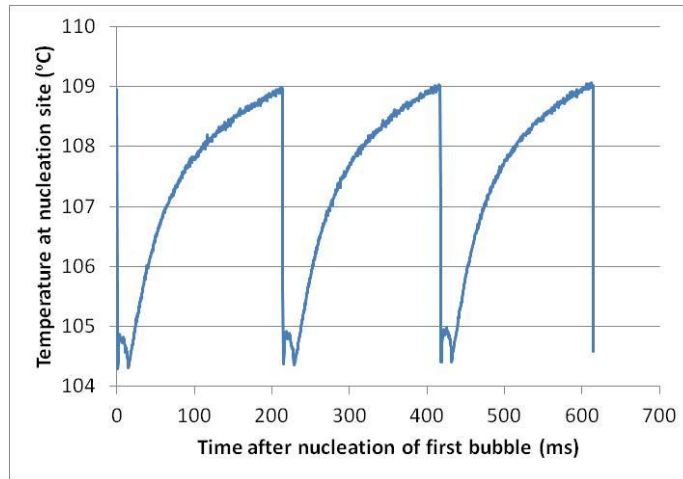


Figure 7 – Temperature history of the nucleation site of interest in Dataset 1. Note the very fast growth period (temperature drop) and relatively slow thermal boundary layer reconstruction exhibiting the characteristic square-root-of-time behavior. The accuracy of measured temperature is $\pm 2^{\circ}\text{C}$; the precision is $< 0.5^{\circ}\text{C}$. (error bars not shown)

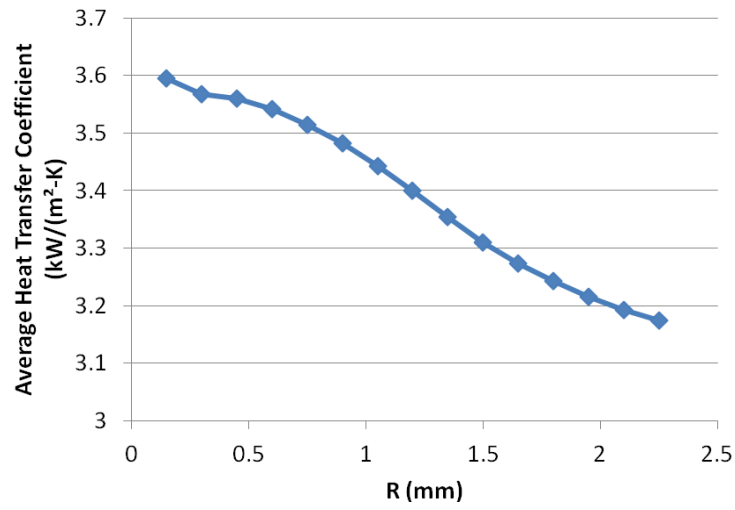
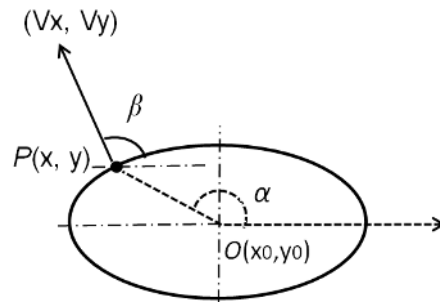
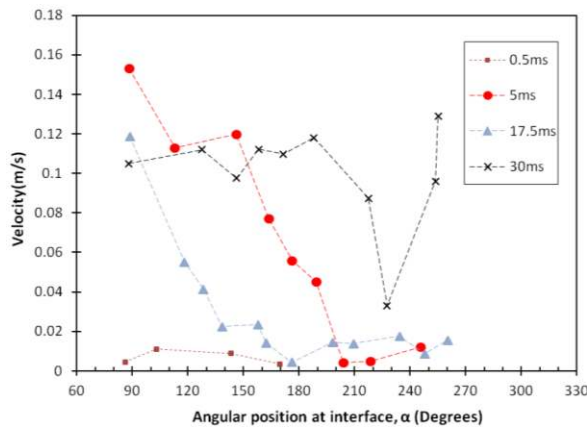


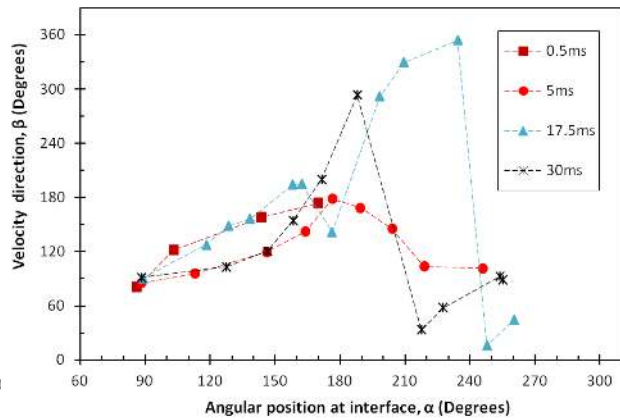
Figure 8 – Average heat transfer coefficient as a function of the radial size of the domain over which the average is calculated. Average of 3 bubbles in Dataset 1. Accuracy of calculated heat transfer coefficient is $\pm 0.8 \text{ kW/m}^2\text{K}$; the precision is $< 0.2 \text{ kW/m}^2\text{K}$. (error bars not shown)



(a) Illustration of parameters



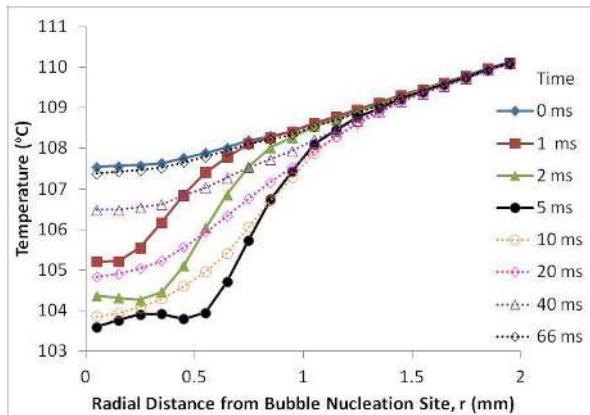
(b)



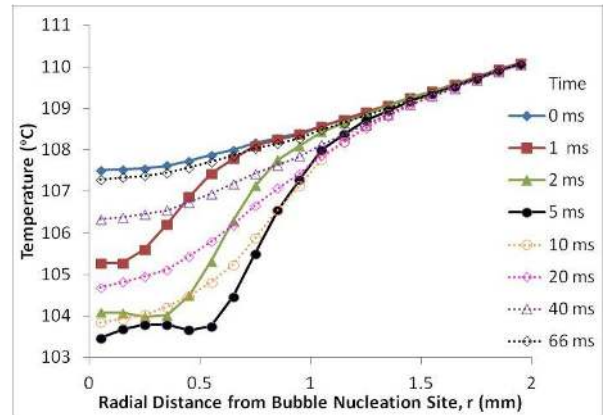
(c)

Figure 9 – Fluid velocity magnitude (b) and direction (c) along the Bubble 1 interface, as defined in (a).

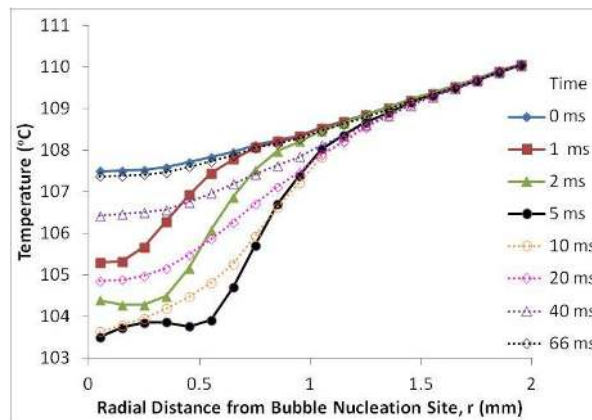
Accuracy of the velocity magnitude measurement is ± 3 mm/s and accuracy of the velocity direction is 0.6 degrees. (error bars not shown)



(a) Bubble 1



(b) Bubble 2



(c) Bubble 3

Figure 10 – Variations of heater surface temperature beneath three consecutive bubbles in Dataset 2. The accuracy of measured temperature is $\pm 2^{\circ}\text{C}$; the precision is $< 0.5^{\circ}\text{C}$. (error bars not shown)

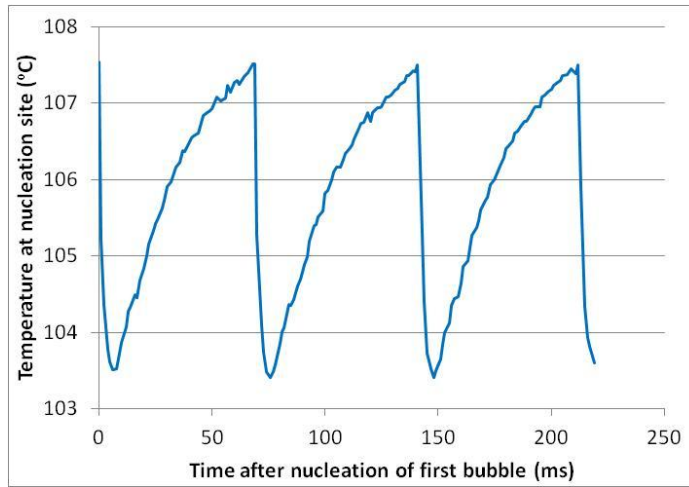


Figure 11 - Temperature history of the nucleation site of interest in Dataset 2. The accuracy of measured temperature is $\pm 2^{\circ}\text{C}$; the precision is $<0.5^{\circ}\text{C}$. (error bars not shown)

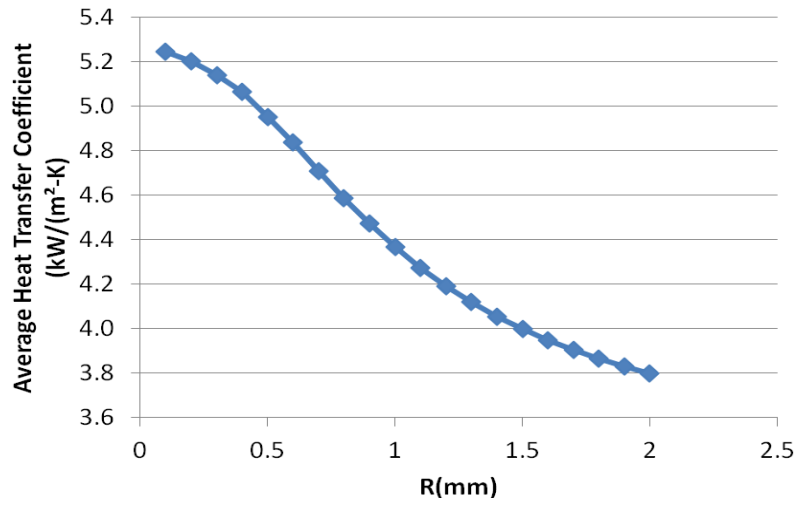


Figure 12 – Average heat transfer coefficient as a function of the radial size of the domain over which the average is calculated. Average of 3 bubbles in Dataset 2. Accuracy of calculated heat transfer coefficient is ± 0.9 kW/m²K; the precision is < 0.2 kW/m²K. (error bars not shown)

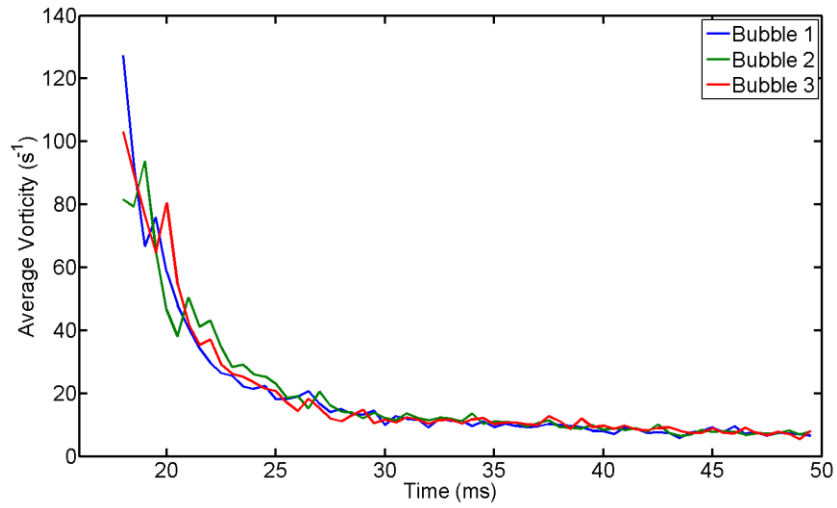


Figure 13 – Absolute value of average z-component of the vorticity vector for Dataset 2 as a function of time after bubble nucleation (bubble departure occurs at t=16 ms). The vorticity was calculated using a central difference approach and averaged over an area of 1.1 mm x 2.2 mm with the bottom corner 0.1 mm to the left and 0.1 mm above the nucleation site. Uncertainty on the calculated values of vorticity is estimated to be ~18%. (error bars not shown)